On the stability of underground caves in calcareous rocks due to long-term weathering

Mánica, Miguel A. ; Ciantia, Matteo; Gens, Antonio

Published in:
Rock Mechanics and Rock Engineering

DOI:
10.1007/s00603-020-02142-y

Publication date:
2020

Document Version
Peer reviewed version

On the stability of underground caves in calcareous rocks due to long-term weathering

Miguel A. Mánica · Matteo O. Ciantia · Antonio Gens

Received: date / Accepted: date

Abstract This paper addresses the problem of the stability of structures on calcareous rocks due to long-term weathering processes. The case study consists of a building resting on a calcarenite rock formation where two abandoned man-made caves exist directly under the structure. The boundaries of the caves were exposed to a slightly acidic environment inducing time-dependent weathering. Analyses were performed following a semi-decoupled approach, where the weathering process, driven by a reactive transport mechanism, was first solved and its results were fed to the mechanical problem which hence accounted for the spatial and temporal evolution or rock damage. For the mechanical problem, a nonlocal constitutive model was employed for the objective simulation of localised deformations. Relevant outcomes are obtained regarding the evolution of the structure's stability and about the importance of regularising the finite element solution in the presence of brittle materials.

Keywords weathering · calcareous rock · stability · nonlocal plasticity · localisation

Miguel A. Mánica
Institute of Engineering, National Autonomous University of Mexico, Mexico City, Mexico
E-mail: mmanicam@iingen.unam.mx

Matteo O. Ciantia
School of Science and Engineering, University of Dundee, Dundee, UK
E-mail: m.o.ciantia@dundee.ac.uk

Antonio Gens
Department of Civil and Environmental Engineering, Universitat Politècnica de Catalunya, Barcelona Tech, Spain
E-mail: antonio.gens@upc.edu

Abbreviations

BVP	Boundary value problem
CHM	Chemo-hydro-mechanical
GDP	Grain dissolution process
HMC	Hyperbolic Mohr-Coulomb
LTD	Long-term debonding
STD	Short-term debonding

List of symbols

B	Parameter in f_{d}
$\mathrm{CaCO_{3(s)}}$	Calcium carbonate species in the solid phase
D	Isotropic diffusion coefficient
D_{ij}	Diffusion tensor
E	Young's modulus
$\mathrm{H_3O^+_{(aq)}}$	Acid ions
J_2	Second invariant of the deviatoric stress tensor
K	Darcy isotropic permeability
K_1, K_2	Reaction rate constants
M	Mass
N_{G}	Number of Gauss points
S_{r}	Degree of saturation
$S_{\mathrm{r,cr}}$	Minimum S_{r} for all the depositional bonds to suspend
Y	Weathering function
Y_{dis}	Component of the weathering function for the LTD process
Y_{sus}	Component of the weathering function for the STD process
a_ϕ	Constant controlling the curvature of the hyperbolic hardening function
b_c	Softening rate for the cohesion and tensile strength

b_ϕ	Softening rate for the friction angle
c^*	Asymptotic cohesion
c^*_{ini}	Initial asymptotic cohesion
$c^*_{\text{ini,uw}}$	Initial asymptotic cohesion for $\xi_{\text{dis}} = 0$
f	Yield function
f_{d}	Function defining the shape of f in the deviatoric plane
l_{s}	Length scale parameter
m	Parameter in f_{d}
n	Effective porosity
p	Mean stress
pH	Potential of the hydrogen
p_t	Isotropic tensile strength
$p_{t\text{ini}}$	Initial isotropic tensile strength
$p_{t\text{ini,uw}}$	Initial isotropic tensile strength for $\xi_{\text{dis}} = 0$
q_i	Component of the real seepage velocity along the i axis
r_{kl}	Radial distance between the kth and lth Gauss points
s_{ij}	Deviatoric stress tensor
w	Normalised averaging factor
w_0	Weighting function
α	Parameter in f_{d}
δ_{ij}	Kronecker delta
ϵ_1	Major principal strain
ϵ_3	Minor principal strain
$\epsilon^{\text{p}}_{\text{eq}}$	Equivalent plastic strain
$\bar{\epsilon}^{\text{p}}_{\text{eq}}$	Nonlocal equivalent plastic strain
ϵ^{p}_{ij}	Plastic strain tensor
ϵ_{s}	Shear strains
θ	Lode's angle
ν	Poisson's ratio
ξ_{dis}	Normalised dissolved mass
$\xi_{\text{dis,cr}}$	Corresponds to ξ_{dis} when all diagenetic bonds have been dissolved
$\sigma^{\text{d}}_{\text{c0}}$	Uniaxial compression strength under dry conditions
$\sigma^{\text{w}}_{\text{c0}}$	Uniaxial compression strength under wet conditions
σ_{ij}	Stress tensor
ϕ^*	Asymptotic friction angle
ϕ^*_{ini}	Initial asymptotic friction angle
ϕ^*_{peak}	Peak asymptotic friction angle
ϕ^*_{res}	Residual friction angle
χ	Value of $\epsilon^{\text{p}}_{\text{eq}}$ separating the hardening and softening regimes
ψ	Angle of dilation
ω	Constant controlling the volumetric component of plastic deformations
$[\cdot]$	Bulk fluid concentrations

1 Introduction

In contact with atmospheric conditions, rocks are subjected to weathering: a complex physicochemical process inducing continuous changes in their properties and composition and, ultimately, leading to the complete disintegration of the rock. From an engineering standpoint, weathering induce a continuous reduction of the mechanical properties having major implications on the stability of structures (Castellanza et al., 2018; Ciantia et al., 2018).

Calcarenites are particularly susceptible to weathering. They can lose instantly up to 60% of their dry strength when their pores are filled with water and, if they remain saturated, their strength continues decreasing due to the dissolution of the bonds and grains in the long-term (Ciantia and Hueckel, 2013; Ciantia et al., 2013). Consequently, a structure resting on calcareous rocks, exposed to atmospheric conditions, may experience large displacements, or even collapse, due to this degradation of the mechanical properties (Parise and Lollino, 2011). Therefore, the prediction of this phenomenon, as well as its implications on the mechanical behaviour, are of uttermost importance. In this regard, considerable progress has been made in recent years in studying the interactions between soil and rock masses and the environment (Gens, 2010). The classical elastoplasticity framework has been extended to accommodate the mechanical and chemical degradation of bonded soils and rocks (Ciantia and di Prisco, 2016; Gajo et al., 2019; Nova et al., 2003; Tamagnini et al., 2002; Tamagnini and Ciantia, 2016; Witteveen et al., 2013), and coupled chemo-hydro-mechanical (CHM) simulations have been performed to study the effect of weathering in engineering problems (Ciantia et al., 2018).

On the other hand, calcarenites might exhibit brittle behaviour with a rapid decrease in their strength after peak under mechanical loading. Ductile behaviour can also be observed depending on factors such as the confining pressure (Zimbardo, 2016; Lagioia and Nova, 1995), the distribution of cement (Lollino and Andriani, 2017), temperature or saturation conditions (Nicolas et al., 2016), and their microstructure (Wong and Baud, 2012). If brittle behaviour predominates in a particular engineering situation, strain-softening will generally result in a non-homogeneous strain field and deformations will tend to localise in the form of shear fractures or compaction bands (Raynaud et al., 2012; Lollino and Andriani, 2017; Baxevanis et al., 2006). However, the numerical simulation of these phenomena, under the framework of continuum mechanics, embodies an intrinsic difficulty. In the presence of softening

materials, continuum approaches deliver non-objective results in the form of a strong dependence with the employed mesh (de Borst et al., 1993). Vanishing energy dissipation and localisation into a region of vanishing volume are obtained as the size of elements is reduced (Pijaudier-Cabot and Bažant, 1987). They also exhibit poor convergence properties (Summersgill et al., 2017) and sensitivity to the alignment of elements (Regueiro and Borja, 2001). Discrete methods (Utili and Crosta, 2011; Potyondy and Cundall, 2004; Kozicki and Donzé, 2008), or the combination of continuum and discrete approaches (Oñate and Rojek, 2004; Morris et al., 2006; Mahabadi et al., 2012), are quite promising alternatives to assess the localisation behaviour of brittle soils and rocks. However, their application to boundary value problems (BVP) of real engineering situations is still not generalised. Continuum approaches can still be used if enriched with some characteristic length (Bažant and Jirásek, 2002). Different strategies, usually called *regularisation techniques*, exist in the literature controlling the size of the localised region and preventing the pathological dependence with the employed mesh. Among them, the nonlocal approach is an attractive alternative since it operates at a constitutive level and, therefore, it does not require the modification of the formulation employed to solve the balance equations. In general, a nonlocal model is one where the behaviour of a material point (or a Gauss point in the context of finite element analyses) does not depend only on its state but also on the state of neighbouring points. Recent examples of application in the simulation of brittle soils and soft rocks can be found in Galavi and Schweiger (2010), Summersgill et al. (2017), Mánica et al. (2018), or Monforte et al. (2019).

This paper addresses the problem of the stability of structures resting on calcareous rocks due to long-term weathering processes. In particular, a 2D plane strain problem is investigated consisting of a building resting on a calcarenite where two abandoned man-made caves exist directly under the structure, a few meters below the ground surface. The caves' boundaries were exposed to an acidic environment, inducing time-dependent weathering. As a first approximation to the problem, a semi-decoupled approach was adopted. The reactive transport simulations were performed independently following the solution strategy from Fernandez-Merodo et al. (2007). These simulations resulted in different spatial distributions in time of the dissolved mass of calcium carbonate which in turn is related to the degradation of inter-particle bonds (Ciantia and di Prisco, 2016). The dissolved mass was translated into reduced strength parameters using the weathering function from Ciantia and di Prisco (2016), and they were applied independently to each Gauss point of the mechanical model. For each weathering scenario, the structure was brought to failure, and the ultimate capacity was assessed in terms of the load-displacement curve. Since the failure phase involved the brittle behaviour of the rock under mechanical loading, the constitutive model employed was regularised following a nonlocal approach for avoiding mesh dependency issues. Relevant outcomes are obtained regarding the evolution of the structure's stability due to long-term weathering. In addition, the importance of regularising the finite element solution for stability analyses, in the presence of brittle materials, is demonstrated.

2 Constitutive and numerical modelling of weathering and mechanical degradation

In the absence of a coupled CHM model regularised to simulate localised deformations objectively, the effects of weathering on the stability of the analysed case are addressed following a semi-decoupled two-step approach. First, the reactive transport problem is solved to derive the spatial and temporal evolution of calcium carbonate concentration. Then, by relating the obtained concentration to the level of bonding, strength parameters are obtained for different times and used in the stability assessment of the structure. The formulation employed to solve the reactive transport problem, the relationship between the derived concentration and the strength, and the employed mechanical constitutive model are briefly described below.

2.1 Transport of chemical species in porous media

The reactive transport simulation was performed using the algorithm put forward by Fernandez-Merodo et al. (2007). The effects of chemical reactions on solute transport were included in the advection-dispersion equation through a chemical sink/source term. It was assumed that the reaction governing the dissolution of calcium carbonate, forming the porous carbonate rock, is given by the following global equation:

$$\mathrm{CaCO_{3(s)}} + 2\mathrm{H_3O^+_{(aq)}} \Longleftrightarrow \mathrm{Ca^{2+}_{(aq)}} + 3\mathrm{H_2O_{(aq)}} + \mathrm{CO_{2(g)}} \quad (1)$$

where subscripts g, aq, and s refer to gas, aqueous, and solid phases respectively. The calcium carbonate species in the solid phase ($\mathrm{CaCO_{3(s)}}$) is assumed to be fixed while the acid ions ($\mathrm{H_3O^+_{aq}}$) are mobile. Then, the

balance equation for both species can be written as

$$\frac{\partial \left[\mathrm{H_3O^+}\right]}{\partial t} = \frac{\partial}{\partial x_i}\left(D_{ij}\frac{\partial \left[\mathrm{H_3O^+}\right]}{\partial x_j}\right) - \frac{\partial}{\partial x_i}\left(q_i \left[\mathrm{H_3O^+}\right]\right) - K_1 \left[\mathrm{CaCO_3}\right] \quad (2)$$

$$\frac{\partial \left[\mathrm{CaCO_3}\right]}{\partial t} = -K_2 \left[\mathrm{H_3O^+}\right] \quad (3)$$

where q_i is the component of the real seepage velocity along the i axis, D_{ij} is a diffusion tensor incorporating the effects of dispersion, K_1 and K_2 are two constants characterising the reaction rate, and $[\cdot]$ indicates the amount of chemical concentration (i.e. solute mass per unit volume of water). Further details on the solution strategy and the algorithm employed are given in (Fernandez-Merodo et al., 2007).

2.2 Effect of weathering on the mechanical behaviour

The effect of bonding was accommodated into the classical elastoplasticity framework by Nova (1986) and Gens and Nova (1993). This work was later extended by Nova et al. (2003) to incorporate the effect of weathering and chemical degradation through the definition of a weathering function, describing the shrinkage of the yield surface due to non-mechanical processes. The weathering function was recently redefined in the model of Ciantia and di Prisco (2016) using a multiscale approach. It distinguishes between two types of bonding in calcarenites: depositional and diagenetic (Ciantia and Hueckel, 2013; Ciantia et al., 2015a). The first type is related to the calcite powder that falls into suspension during water inundation (during saturation). The second type are stronger bonds that are only affected by long-term dissolution processes. This definition allowed describing the weathering function using physical quantities such as the degree of saturation S_r and the relative amount of dissolved calcium carbonate

$$\xi_\mathrm{dis} = \frac{\Delta M}{M_0} = \frac{\left[\mathrm{CaCO_3}\right]_0 - \left[\mathrm{CaCO_3}\right]}{\left[\mathrm{CaCO_3}\right]_0} \ . \quad (4)$$

In this way, the model takes into account the process of debonding induced by both the saturation of the material (short-term debonding, STD) and the dissolution of diagenetic bonds caused by the ionic composition of the bulk fluid (long-term debonding, LTD) (Fig. 1). Then, the weathering function, controlling the evolution of the strength, can be defined as

$$Y = Y_\mathrm{sus} + Y_\mathrm{dis} \quad (5)$$

where

$$Y_\mathrm{sus} = \begin{cases} \dfrac{\sigma_{\mathrm{c}0}^\mathrm{d} - \sigma_{\mathrm{c}0}^\mathrm{w}}{\sigma_{\mathrm{c}0}^\mathrm{d}}\left(1 - \dfrac{S_\mathrm{r}}{S_\mathrm{r,cr}}\right)^2 & \text{if } S_\mathrm{r} \le S_\mathrm{r,cr} \\ 0 & \text{if } S_\mathrm{r} > S_\mathrm{r,cr} \end{cases} \quad (6)$$

$$Y_\mathrm{dis} = \begin{cases} \dfrac{\sigma_{\mathrm{c}0}^\mathrm{w}}{\sigma_{\mathrm{c}0}^\mathrm{d}}\left(1 - \dfrac{\xi_\mathrm{dis}}{\xi_\mathrm{dis,cr}}\right)^2 & \text{if } \xi_\mathrm{dis} \le \xi_\mathrm{dis,cr} \\ 0 & \text{if } \xi_\mathrm{dis} > \xi_\mathrm{dis,cr} \end{cases} \quad (7)$$

where $\sigma_{\mathrm{c}0}^\mathrm{w}$ and $\sigma_{\mathrm{c}0}^\mathrm{d}$ are the uniaxial compression strength of calcarenite rock under wet and dry conditions respectively, $S_\mathrm{r,cr}$ is the minimum degree of saturation required for all depositional bonds to suspend, and $\xi_\mathrm{dis,cr}$ is the normalised dissolved mass when all bonds have been dissolved. The model of Ciantia and di Prisco (2016) also considers the effect of weathering on the stiffness degradation using a damage mechanics framework and weathering functions similar to Eq. (5) to (7) to define the damage variable.

The model of Ciantia and di Prisco (2016) has been employed in 2D and 3D CHM finite element simulations (Ciantia et al., 2018), by using an innovative coupling strategy between the codes solving the reactive transport problem (section 2.1) and the hydro-mechanical problem. However, the study of the stability conditions of structures on calcareous rocks requires dealing with the issue of strain localisation. Therefore, a different constitutive model is employed here, able to simulate localised deformations objectively. The weathering function, from Eq. (5) to (7), is only employed here to derive the strength parameters for the considered weathering scenarios.

2.3 Nonlocal mechanical degradation

The constitutive model employed here to assess the degradation of the calcarenite under mechanical loading corresponds to that described in Mánica et al. (2018). Although it was intended for clayey rocks, it shares the same principle than the mechanical part of the model in Ciantia and di Prisco (2016) for carbonate rocks: plastic deformations can cause the degradation and breakage of interparticle bonds. In addition, the model is able to simulate localised deformations objectively through the incorporation of a nonlocal regularisation preventing the pathological dependence with the employed mesh. Only a brief description is presented here; for further details see Mánica et al. (2018).

The model is formulated within the framework of elastoplasticity. Inside the yield surface, the response

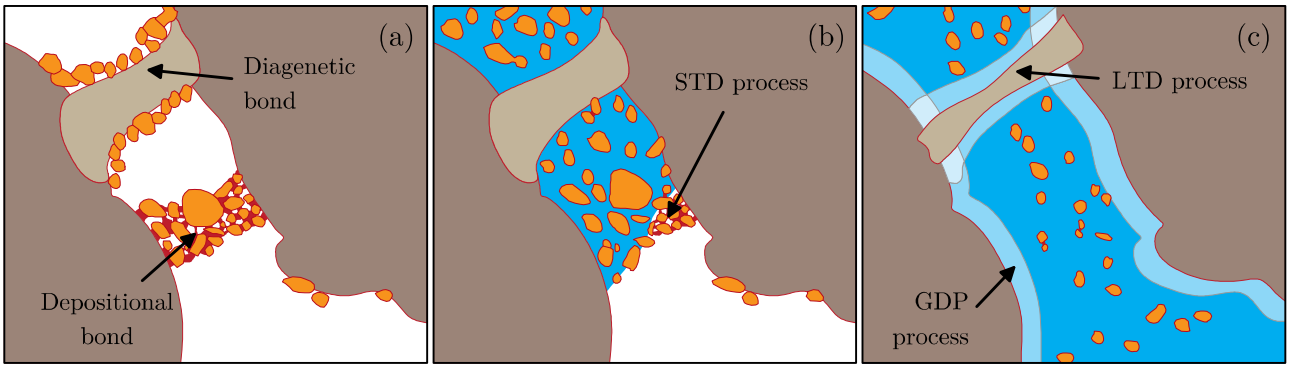

Fig. 1 Microscopic weakening process: (a) initial bonded state, (b) saturation-induced short-term debonding (STD) of depositional bonds, and (c) dissolution-driven long-term debonding (LTD) and grain dissolution process (GDP).

is assumed linear elastic and characterised by Hooke's law. The yield function is defined by a hyperbolic approximation of the Mohr-Coulomb (HMC) criterion (Gens et al., 1990) expressed as

$$f = \sqrt{\frac{J_2}{f_{\mathrm{d}}(\theta)} + \left(c^* + p_t \tan\phi^*\right)^2} - \left(c^* + p \tan\phi^*\right) \tag{8}$$

where c^* is the asymptotic cohesion, ϕ^* is the asymptotic friction angle, p_t is the isotropic tensile strength, p is the mean stress, J_2 is the second invariant of the deviatoric stress tensor $s_{ij} = \sigma_{ij} - p\ \delta_{ij}$ (where δ_{ij} is the Kronecker delta), θ is the Lode's angle, and f_{d} is a function expressed by Eq. (9), defining the shape of f in the deviatoric plane (van Eekelen, 1980).

$$f_{\mathrm{d}}(\theta) = \alpha\left(1 + B\sin 3\theta\right)^m \tag{9}$$

where α, B, and m are function's parameters, and where $m = -0.229$ and $B = 0.85\alpha^{1/2}$ were assumed (van Eekelen, 1980). Isotropic hardening/softening is accounted through the evolution of strength parameters with plastic deformation as follows:

$$\tan\phi^* = \begin{cases} \tan\phi^*_{\mathrm{ini}} + \dfrac{\epsilon^{\mathrm{p}}_{\mathrm{eq}}}{a_\phi + \dfrac{\epsilon^{\mathrm{p}}_{\mathrm{eq}}}{\Delta_\phi}} & \text{if } \epsilon^{\mathrm{p}}_{\mathrm{eq}} \le \chi \\ \tan\phi^*_{\mathrm{peak}} - \left(\tan\phi_{\mathrm{peak}} - \tan\phi^*_{\mathrm{res}}\right)\left[1 - \mathrm{e}^{-b_\phi\left(\epsilon^{\mathrm{p}}_{\mathrm{eq}} - \chi\right)}\right] & \text{if } \epsilon^{\mathrm{p}}_{\mathrm{eq}} > \chi \end{cases} \tag{10}$$

$$\Delta_\phi = \frac{\chi}{\dfrac{\chi}{\tan\phi^*_{\mathrm{peak}} - \tan\phi^*_{\mathrm{ini}}} - a_\phi} \tag{11}$$

$$c^* = \begin{cases} c^*_{\mathrm{ini}} & \text{if } \epsilon^{\mathrm{p}}_{\mathrm{eq}} \le \chi \\ c^*_{\mathrm{ini}}\mathrm{e}^{-b_c\left(\epsilon^{\mathrm{p}}_{\mathrm{eq}} - \chi\right)} & \text{if } \epsilon^{\mathrm{p}}_{\mathrm{eq}} > \chi \end{cases} \tag{12}$$

$$p_t = \begin{cases} p_{t\mathrm{ini}} & \text{if } \epsilon^{\mathrm{p}}_{\mathrm{eq}} \le \chi \\ p_{t\mathrm{ini}}\mathrm{e}^{-b_c\left(\epsilon^{\mathrm{p}}_{\mathrm{eq}} - \chi\right)} & \text{if } \epsilon^{\mathrm{p}}_{\mathrm{eq}} > \chi \end{cases} \tag{13}$$

where $\epsilon^{\mathrm{p}}_{\mathrm{eq}}$ is a scalar state variable defined as

$$\epsilon^{\mathrm{p}}_{\mathrm{eq}} = \sqrt{\epsilon^{\mathrm{p}}_{ij}\epsilon^{\mathrm{p}}_{ij}} \tag{14}$$

$\epsilon^{\mathrm{p}}_{ij}$ is the plastic strain tensor, χ is the value of $\epsilon^{\mathrm{p}}_{\mathrm{eq}}$ separating the hardening and softening regimes, a_ϕ is a constant controlling the curvature of the hyperbolic hardening function, b_ϕ controls the softening rate for the friction angle, and b_c controls the softening rate for the cohesion and tensile strength. The subscripts *ini*, *peak*, and *res* refer to the initial, peak, and residual yield envelopes respectively. The flow rule is directly obtained from the yield criterion as follows:

$$\frac{\partial g}{\partial \sigma_{ij}} = \omega\frac{\partial f}{\partial p}\frac{\partial p}{\partial \sigma_{ij}} + \frac{\partial f}{\partial J_2}\frac{\partial J_2}{\partial \sigma_{ij}} + \frac{\partial f}{\partial \theta}\frac{\partial \theta}{\partial \sigma_{ij}} \tag{15}$$

where ω is a constant controlling the volumetric component of plastic deformations. A non-associated flow rule is considered here and, therefore, $\omega \neq 1$.

The nonlocal extension of the model is obtained by replacing the local state variable in Eq. (14) by its nonlocal counterpart $\bar{\epsilon}^{\mathrm{p}}_{\mathrm{eq}}$, obtained through a weighted average of the local state variable at neighbouring points. In the actual implementation, $\bar{\epsilon}^{\mathrm{p}}_{\mathrm{eq}}$ is computed as

$$\bar{\epsilon}^{\mathrm{p}}_{\mathrm{eq}k} = \sum_{l=1}^{N_{\mathrm{G}}} w_{kl}\epsilon^{\mathrm{p}}_{\mathrm{eq}l} \tag{16}$$

where N_{G} is the number of Gauss point within a radius of $2l_{\mathrm{s}}$ from the kth Gauss point (Galavi and Schweiger, 2010), w_{kl} is the normalised averaging factor defined as

$$w_{kl} = \frac{w_{0kl}(r_{kl})}{\sum_{m=1}^{N_{\mathrm{G}}} w_{0km}(r_{km})}\ . \tag{17}$$

r_{kl} is the radial distance between the kth and the lth Gauss points,

$$w_{0kl}(r_{kl}) = \frac{r_{kl}}{l_s} e^{-\left(\frac{r_{kl}}{l_s}\right)^2} \quad (18)$$

is the special weighting function put forward by Galavi and Schweiger (2010), and l_s is a length scale parameter controlling the size of the interaction radius ($2l_s$) and, in turn, the size of the localised region. The nonlocal state variable is computed only for points in the softening regime; in the hardening regime the model is assumed local.

The model has been implemented as a user-defined model in the finite element code Plaxis (Brinkgreve et al., 2019), which was employed to assess the stability of the building for different weathering scenarios.

3 Parameters employed and mesh independence

3.1 Local constitutive model

The strength parameters employed to characterise the considered calcarenite correspond to those calibrated in Ciantia et al. (2018) from laboratory experiments performed on samples retrieved from the site. In that work, experimental results were simulated using the model from Ciantia and di Prisco (2016). The model uses the yield locus proposed by Nova (1992), in which a single function handles yielding under volumetric and deviatoric loading, and it provides flexibility to reproduce more closely the shapes of yield surfaces found experimentally for bonded materials (Gens and Nova, 1993). Fig. 2 shows the adjusted envelopes from Ciantia et al. (2018) for a dry, a saturated, and a saturated weathered calcarenite compared with the experimental results. However, as mentioned in section 2.3, the nonlocal mechanical model employed uses a HMC envelope (Eq. 8) where yielding under volumetric loading is not contemplated. Since the objective of the present work is to evaluate the evolution of the stability of the structure due to long-term weathering, which is assessed by bringing the structure to failure for different weathering scenarios, the yielding/failure mechanism under deviatoric loading is the most relevant one for the present application and, therefore, the use of the HMC surface is considered appropriate. The adjusted envelopes using the HMC are also depicted in Fig. 2 for the same cases. The initial scenario of the case study assumes a saturated condition of the domain from which the effects of a long-term dissolution weathering process are studied. Therefore, the initial peak yield envelope employed corresponds to the blue curve in Fig. 2; a saturated unweathered calcarenite. A summary of the parameters corresponding to this initial condition is presented in Table 1.

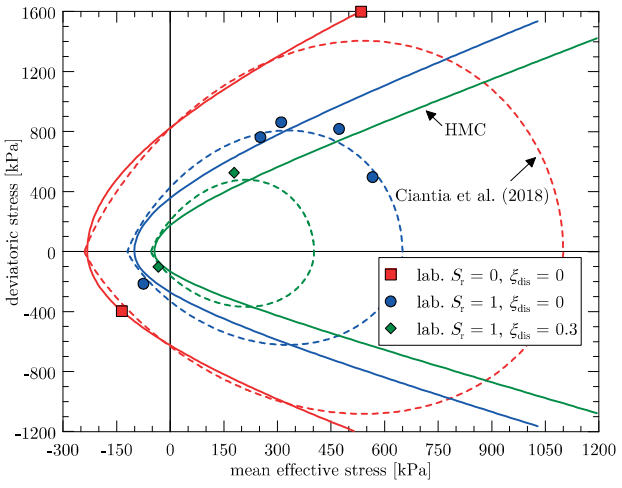

Fig. 2 Experimental (Ciantia et al., 2018) and calibrated yield locus for dry ($S_r = 0$), saturated ($S_r = 1$), and saturated weathered ($S_r = 1$, $\xi_{dis} = 0.3$) calcarenite.

Table 1 Mechanical parameters employed for the intact calcarenite

Parameter	Symbol	Units	Value
Young's modulus	E	[MPa]	250
Poisson's ratio	ν	[-]	0.3
Initial asymptotic friction angle	ϕ^*_{ini}	[°]	15
Peak asymptotic friction angle	ϕ^*_{peak}	[°]	23
Residual friction angle	ϕ^*_{res}	[°]	23
Initial unweathered asymptotic cohesion ($\xi_{dis} = 0$, $S_r = 0/S_r = 1$)	$c^*_{ini,uw}$	[kPa]	830/360
Initial unweathered isotropic tensile strength ($\xi_{dis} = 0$, $S_r = 0/S_r = 1$)	$p_{tini,uw}$	[kPa]	232/100
Equivalent strain at peak strength	χ	[-]	0.0015
Constant in hardening law	a_ϕ	[-]	0.002
Rate of reduction of friction angle	b_ϕ	[-]	0
Rate of reduction of cohesion	b_c	[-]	22
Non-associative constant	ω	[-]	1
Length scale parameter	l_s	[cm]	40

A non-associated flow rule was adopted, following the practical recommendation of $\psi = \phi/3$ for soft rocks (Chandra et al., 2010) where ψ is the angle of dilation. Although the plastic potential does not result in a constant dilation angle, since it depends on stress level and evolves with plastic deformations, $\psi = \phi/3$ can be fairly approximated by assuming $\omega = 0.333$ in Eq. (15).

The remaining stiffness parameters and parameters in the hardening/softening laws were determined through the simulation of unconfined compression tests from Ciantia et al. (2018). The simulations were carried out for a single Gauss point, i.e. assuming only the constitutive behaviour. Obtained results are shown in Fig. 3, along with the laboratory data for a dry and a saturated calcarenite. A reasonable agreement between both can be noted. The derived parameters are given in Table 1. It is important to mention that strain-softening is related here only to the degradation and breakage of inter-particle bonds and, therefore, only the cohesion and tensile strength are reduced due to the accumulation of plastic deformations during mechanical loading. For instance, the friction angle also reduces with deformation in soft rocks (and hard soils) with high clay fraction due to the polishing and reorientation of particles on the failure surface (Gens, 2013). Nevertheless, the rate of this latter reduction is much slower and requires very large deformations. For simplicity, a constant friction angle was assumed here.

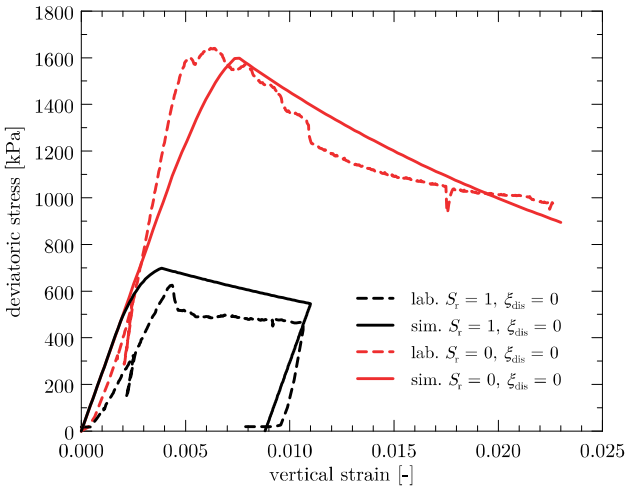

Fig. 3 Experimental (Ciantia et al., 2018) and simulated (single Gauss point integration) unconfined compression test.

3.2 On the length scale parameter and the softening rate

The length scale parameter l_s controls the width of the localised region; in the particular nonlocal regularisation employed, the width of shear bands is roughly equal to l_s (Mánica et al., 2018; Galavi and Schweiger, 2010). The observed width of the localisation process in geomaterials seems to be related with their microstructure (Desrues and Viggiani, 2004), and l_s should be selected accordingly to obtain a similar size than those observed in experiments. However, since a minimum amount of Gauss points are required within the interaction radius to properly compute the nonlocal variable (Galavi and Schweiger, 2010), the simulation of a realistic localisation region would require an excessively refined mesh. This difficulty can be circumvented by assuming that the effects of the actual sheared zone can be merged into a numerical shear band of a larger size. The mesh should be as refined as possible, but without exceeding available computational capacities. Then, l_s should be chosen according to the available mesh, and the softening rate adjusted to obtain the desired global softening response. This technique, known as softening scaling (Mánica et al., 2018; Galavi and Schweiger, 2010; Brinkgreve, 1994), is similar to the crack band theory (Bažant and Oh, 1983) where softening is adjusted with respect to the element size. However, in the latter approach, issues of poor convergence properties and dependence on the orientation of elements persist.

As mentioned in the previous section, the softening rate parameter for the cohesion and tensile strength (b_c) was selected by adjusting stress-strain curves from laboratory data from a constitutive standpoint (Fig. 3). However, it is important to notice that the obtained value b_c will be, to a large extent, arbitrary and might result in a gross misprediction of the capacity of a given BVP analysed, as shown later. The conventional interpretation ceases to be objective in the softening branch due to the formation of fractures or shear surfaces resulting in non-homogeneous stress/strain fields. Furthermore, as mentioned above, the softening rate is related to the selected length scale parameter for a nonlocal regularisation. A more appropriate approach would be to simulate a given laboratory test as a BVP, using a nonlocal regularisation and a given length scale parameter, and to approximate the global load-displacement curve. However, the shape of the latter curve in the softening branch depends on the specific localisation pattern of the test, which can be quite complex in calcarenites. These patterns depend on the particular heterogeneities of the sample and are extremely difficult to represent in a simulation, particularly for cylindrical samples. Moreover, they are generally not reported in the literature.

The proposal of a rational approach to determine an adequate softening rate for nonlocal simulations of real engineering problems, from laboratory test results, is beyond the scope of the present work and more research is required in that regard. Here, the softening rate determined from the calibration at a constitutive level (Fig. 3) was adopted in the simulations described below. However, being aware of the uncertainty introduced, analyses were also performed with different values of b_c to assess its influence on the results.

3.3 Mesh independence

To demonstrate the importance of regularising the finite element solution in the presence of brittle materials, a series of unconfined biaxial test simulations were performed, with the parameters derived above, using different meshes with varying element sizes. The dimensions of the models were large enough to contain the expected numerical shear bands according to $l_s = 40$ cm, employed in the case study (later described); they were 8 m high and 4 m wide. Analyses were performed with meshes of 88, 126, 256, 484, 1024, and 1556 elements and with the local and nonlocal versions of the mechanical model. In the case of the nonlocal model, analyses were only performed for the meshes with 484, 1024, and 1556 elements to fulfil the criterion

$$l_s \geq L_{el} \tag{19}$$

where L_{el} is the maximum length of an element in the finite element mesh. The criterion guarantees a sufficient amount of Gauss points within the interaction

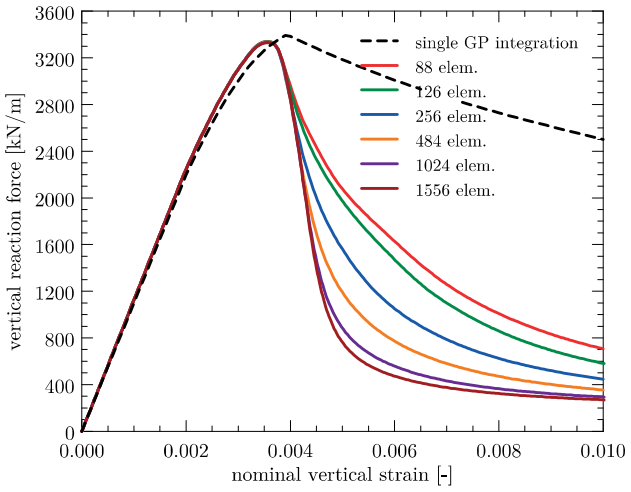

Fig. 4 Vertical reaction force vs nominal vertical strain of biaxial test for different meshes with the local model and from a single Gauss point integration.

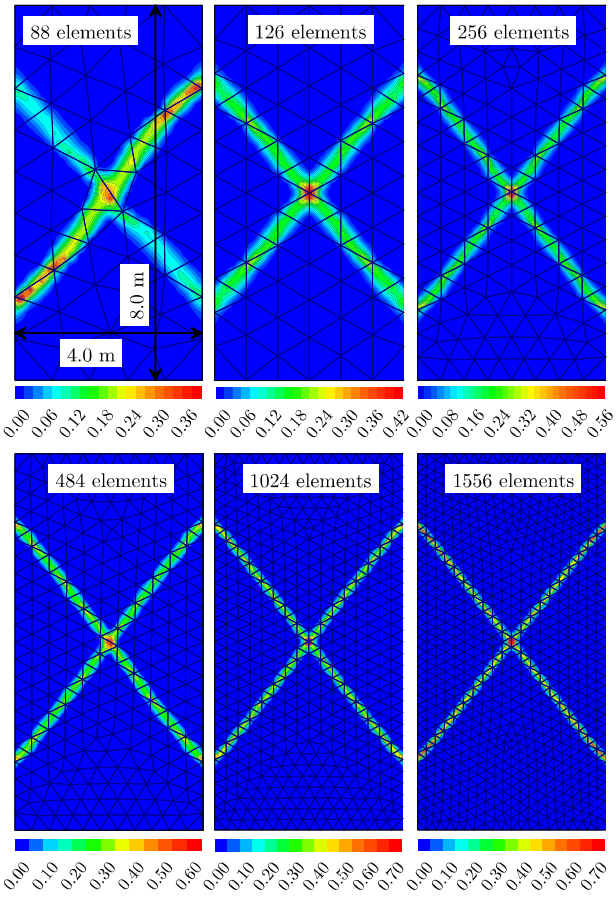

Fig. 5 Contours of shear strain of biaxial test for different meshes with the local model.

radius to properly compute the nonlocal state variable (Galavi and Schweiger, 2010). Loading was applied under displacement control, and fixed horizontal displacements were prescribed at the bottom and top boundaries to generate a non-uniform stress/strain field and favour the onset of localisation. The obtained response for the local model is depicted in Fig. 4 in terms of the vertical reaction force (per unit width) vs the nominal vertical strain (computed from the displacement of the top boundary and the initial height). It is evident that the local model delivers non-objective results, showing an increasingly brittle response of the BVP as the number of elements is increased (i.e. as their size is reduced), even though they all share the same constitutive behaviour (also depicted in Fig. 4). By increasing the number of elements, the response tends towards a vertical drop after the peak, which corresponds to the limiting situation allowed by the displacement driven formulation employed. Mesh dependence is also evident in Fig. 5, showing the contours of shear strain $\epsilon_s = (\epsilon_1 - \epsilon_3)/2$, which are an excellent means to ob-

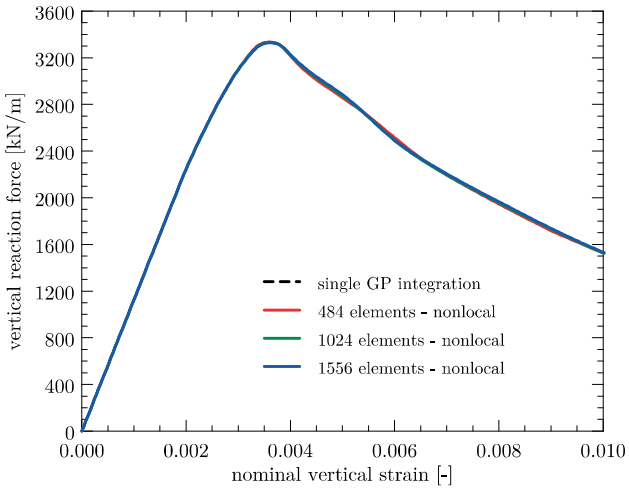

Fig. 6 Vertical reaction force vs nominal vertical strain of biaxial test for different meshes with the nonlocal.

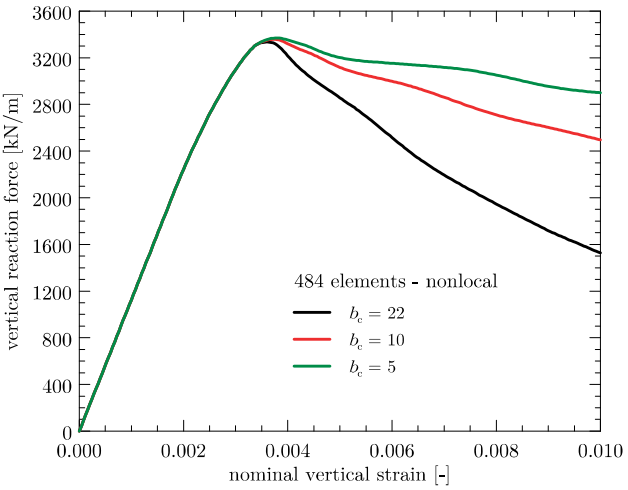

Fig. 8 Vertical reaction force vs nominal vertical strain of biaxial tests with the nonlocal model and for different values of b_c.

serve the configuration of localised plastic deformations (Mánica et al., 2018). Although the localisation pattern is similar, the thickness of shear bands reduces with element size, and it is approximately equal to the width of a single element. On the other hand, objectivity was restored using the nonlocal approach resulting in a single force vs nominal strain curve (Fig. 6) and the same configuration and thickness of shear bands (Fig. 7) regardless of the mesh employed.

As previously mentioned, analyses were also performed for the nonlocal model with different values of b_c, equal to 10 and 5. The obtained force vs nominal strain curves are depicted in Fig. 8 for the mesh with 484 elements. As expected, less brittle behaviour is obtained in the BVP by reducing the constitutive softening rate. However, it is important to notice that, regardless of the softening rate employed, and even in the case of the non-objective local simulations (Fig. 4), the peak load is approximately the same and only the post-peak behaviour differs among the different analyses. The same outcome has been observed in other simulations of biaxial tests involving brittle materials (Summersgill et al., 2017; Mánica et al., 2018).

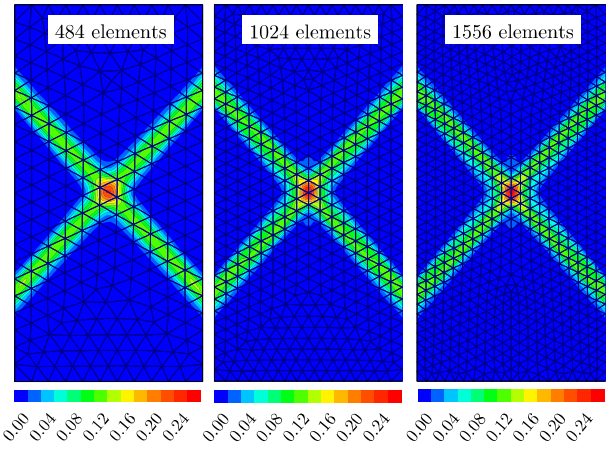

Fig. 7 Contours of shear strain of biaxial tests for different meshes with the nonlocal model.

4 Application to the stability analysis of a building resting on a calcarenite

4.1 Model setup

The geometry and boundary conditions of the case study are depicted in Fig. 9. They correspond to a simplified 2D version (plane strain) of a real structure resting on a calcarenite deposit in the urban area of Canosa di Puglia, where two abandoned man-made caves exist directly under the building, a few meters below the ground surface. A comprehensive description of the case study can be found in Ciantia et al. (2018, 2015b). In Ciantia et al. (2018), authors performed 2D and 3D coupled chemo-hydro-mechanical simulations to assess the evolution of settlement damage due to long-term weathering process. Because a local constitutive relationship was used, the authors considered only the deformations/settlements away from failure. Here, a detailed simulation of the case study is not intended as the main objective of the present work. The aim is to demonstrate the effect of long-term weathering on the ultimate capacity of a structure as well as to show the

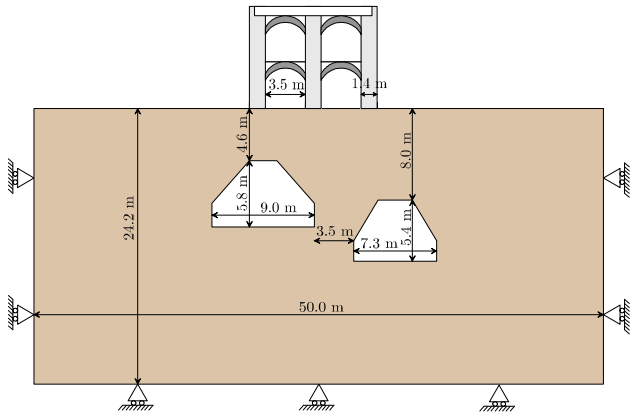

Fig. 9 Geometry and boundary conditions.

importance of regularising the finite element solution when dealing with brittle materials.

As mentioned before, parameters are the same as those employed in the biaxial tests given in Table 1 for a saturated calcarenite, assumed as the initial condition for the ground. Then, different weathering scenarios were considered derived from assuming the exposure of the caves' boundaries to an acidic environment. The reactive transport simulation was performed independently using the approach from Fernandez-Merodo et al. (2007). It assumes a null initial concentration of $[H_3O^+]$ ions in the domain and a fixed concentration, corresponding to a pH of 6.7, imposed on the caves' surfaces as a boundary condition. This concentration gradient propagates into the rock by means of a diffusive phenomenon causing the long-term dissolution of $[CaCO_3]$. Parameters for the reactive transport model are summarised in Table 2. Most of them were taken from Ciantia et al. (2018). The reaction rates were derived by performing dissolution tests (Ciantia, 2013) on the same calcarenite, and the diffusion coefficient was back-calculated through the simulation of a small-scale pillar failure test where the specimen was subjected to long-term exposure to an acidic solution (Ciantia et al., 2018).

Table 2 Parameter for the reactive transport simulation

Parameter	Symbol	Units	Value
Porosity	n	[-]	0.59
Darcy isotropic permeability	K	[m^2]	1e-12
Isotropic diffusion coefficient	D	[m^2/s]	1.16e-7
Reaction rate constant	K_1	[1/s]	-1.0e-10
Reaction rate constant	K_2	[1/s]	-1.6
Initial calcium carbonate concentration	$[CaCO_3]_0$	[mol/m^3]	25190
Acid ions concentration applied on the caves's surface	$[H_3O^+]$	[mol/m^3]	1.65e-4
Corresponding potential of hydrogen	pH	[-]	6.7

Different scenarios were considered corresponding to different times of the reactive transport simulation. Particularly, times equal to 0, 50, 100, 150, 200, and 250 years were adopted. Each scenario resulted in a given spatial distribution of the normalised dissolved mass of calcium carbonate ξ_{dis}; they are depicted in Fig. 10. ξ_{dis} is related to the level of debonding (Ciantia and di Prisco, 2016) and, therefore, to the amount of cohesion and tensile strength. Since an initial saturated condition is being assumed, the short-term debonding process due to saturation is not being considered, and the weathering function reduces to

$$Y = \begin{cases} \left(1 - \dfrac{\xi_{\text{dis}}}{\xi_{\text{dis,cr}}}\right)^2 & \text{if } \xi_{\text{dis}} \leq \xi_{\text{dis,cr}} \\ 0 & \text{if } \xi_{\text{dis}} > \xi_{\text{dis,cr}} \end{cases} . \tag{20}$$

Therefore, only long-term debonding due to the chemical dissolution of diagenetic bonds is being investigated

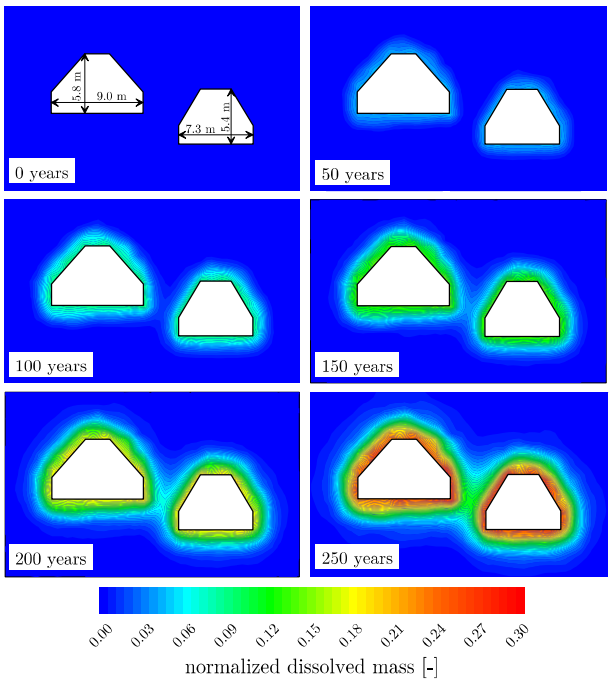

Fig. 10 Normalised dissolved mass for the different weathering scenarios.

here. The value of cohesion and tensile strength, for each weathering scenario, are be given by

$$c^*_{\text{ini}} = Y c^*_{\text{ini,uw}} \tag{21}$$

$$p_{t\text{ini}} = Y p_{t\text{ini,uw}} \tag{22}$$

where $c^*_{\text{ini,uw}}$ and $p_{t\text{ini,uw}}$ are the initial asymptotic cohesion and initial isotropic tensile strength for $\xi_{\text{dis}} = 0$. They are independently assigned to each Gauss point in the model, according to the value of ξ_{dis} obtained in the reactive transport simulations.

For the mechanical simulations of each weathering scenario, initial stress for the free field condition (i.e. without the presence of the caves and the building) were generated from the known unit weight of the rock, estimated equal to 17 kN/m^3, and assuming a coefficient of earth pressure at rest of 0.429. The latter was determined from the adopted Poisson's ratio as

$$K_{\text{o}} = \frac{\nu}{1-\nu} \ . \tag{23}$$

Then, the excavation was simulated by deactivating the solid elements within the caves' boundaries. The latter was performed in two stages: the left cave was excavated first followed by the excavation of the right one. In all cases, equilibrium was reached and little plastic deformations occurred during the excavation stages.

For the unweathered case, different meshes were employed to assess the importance of regularisation. Mesh independence is often assessed in the context of biaxial test simulations (or other laboratory-scale simulations) while the consequences of not regularising the solution are rarely investigated when considering large BVP of engineering situations. The employed meshes are shown in Fig. 11; they comprise 13450, 7902, 3075, 1675, 897, and 429 triangular 15-noded finite elements with fourth-order interpolation and 12 integration points. They are refined in the zone under the foundation and around the caves where plastic deformations take place. All meshes were analysed with the local model, but only those with 13450 and 7902 elements were analysed with the nonlocal approach since they are the only ones that meet the criterion in Eq. (19). It is important to mention that the latter criterion only has to be fulfilled by those elements experiencing plastic deformations and, therefore, larger elements are employed away from the caves to speed up computations.

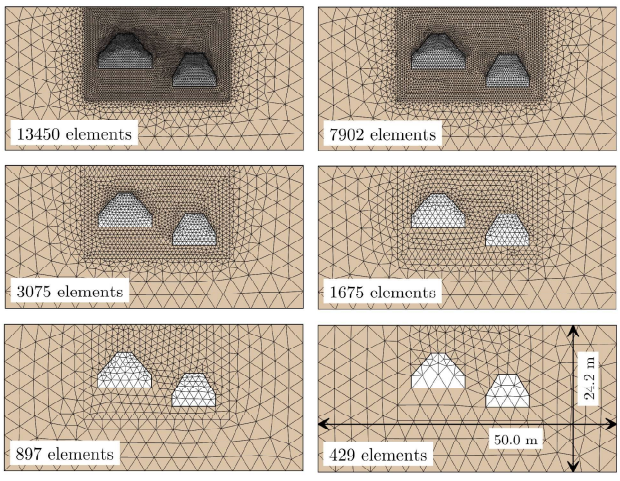

Fig. 11 Employed meshes.

Loading was applied by prescribing a downward vertical displacement of 10 cm at the building foundations, and the ultimate capacity was assessed in terms of the total vertical reaction force (per unit width) vs the applied displacement curve. Although this procedure allows observing the softening branch of the curve, the three foundations settling at the same rate does not represent a realistic loading condition. Therefore, the displacement-controlled analyses were only performed for the unweathered case to assess mesh independence. The remaining analyses were performed under load-control. In the latter case, convergence is only possible until the peak of the load-displacement curve.

4.2 Obtained results - mesh independence in displacement-controlled simulations

The results obtained for the displacement-controlled simulations are shown in Fig. 12, in terms of the vertical

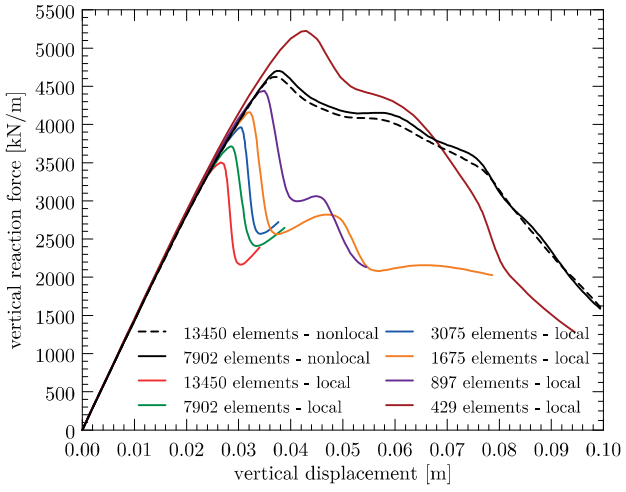

Fig. 12 Vertical reaction force vs applied vertical displacement of the analysed case (unweathered) for different meshes with the local and nonlocal models (displacement-controlled).

reaction force vs the applied displacement, for the local and nonlocal analyses. None of the local analyses were able to apply the 10 cm of displacement prescribed, and convergence issues were encountered at different stages; a common result in the absence of a regularisation technique when dealing with softening materials (Summersgill et al., 2017). A major finding can be identified from the local analyses in Fig. 12. In more constrained BVPs, as in the biaxial test simulations (Fig. 4 and 6), approximately the same peak load is reached, even with the local model, regardless of the number of elements employed; only the post-peak behaviour is mesh-dependent if not regularised. However, in more complex BVPs (as the one analysed here), even the peak load reached shows a pathological dependence with the employed mesh. A higher load is reached as the size of elements is increased; this result has major implications in the evaluation of ultimate limit states of structures resting on brittle materials. On the other hand, only minor differences were obtained between the force-displacement curves of the two nonlocal analysis with different meshes. They showed approximately the same peak load, the same softening behaviour, and no convergences issues were encounter in applying the 10 cm of displacement prescribed.

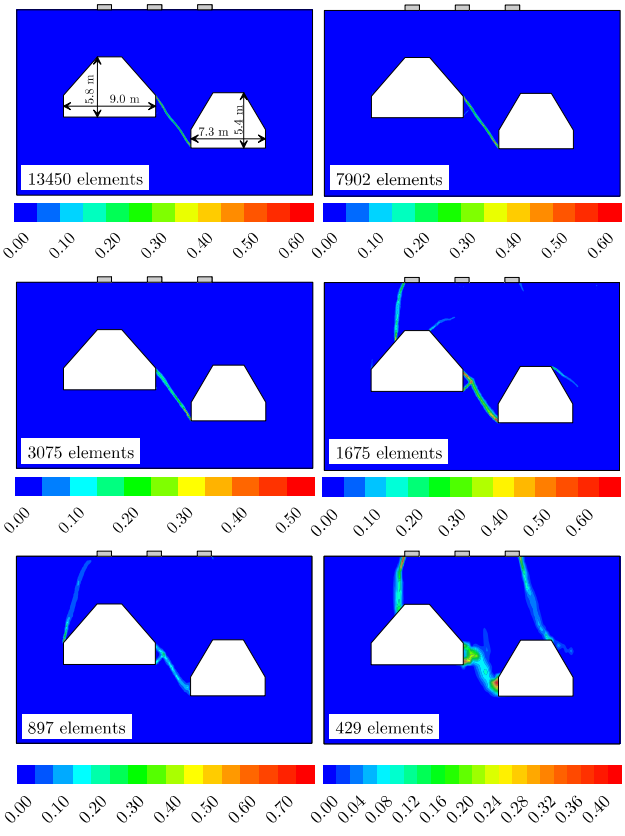

Fig. 13 Contours of shear strain of the analysed case (unweathered) for different meshes with the local model (displacement-controlled).

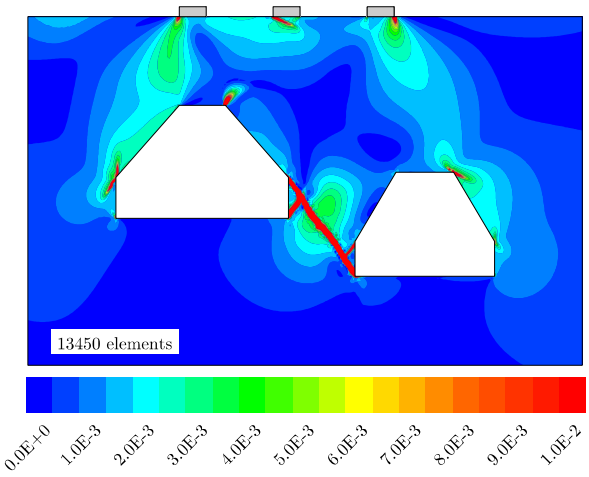

Fig. 14 Contours of shear strain of the analysed case (unweathered) for the mesh with 13450 elements, and with the local model, using a different colour scale (displacement-controlled).

Regarding the configuration of localised deformations, Fig. 13 shows the contours of shear strains for the simulations using the local model when convergence was no longer reached. Mesh dependence can be identified, as in Fig. 5, by the increase in thickness of shear bands as the size of elements increases. In all cases, a shear band forms first in the pillar between the caves. Latter, shear bands appear joining the caves with the ground surface and forming a block moving downward. Nevertheless, the latter is only evident for the mesh with 429 elements, in which it was possible to apply almost fully the prescribed displacement.

Fig. 13 might give the wrong impression that no shear deformations occur apart from the localised areas; however, this is not the case. For instance, Fig. 14 shows the same data than the analysis for the mesh with 13450 elements in Fig. 13 but with a different colour scale, going from 0 to 1% of deformation. Shear deformations occur all around the caves and under the foundation. However, once the problem localises, plastic shear deformations concentrate within the shear bands, forming the failure mechanism, and they become quite large in comparison with areas with no localisation.

Contours of shear strain for the nonlocal analyses are shown in Fig. 15. The same configuration of localised deformations and approximately the same thickness of the shear bands were obtained. The failure mechanism is clearly identified in this case, where a block of material is formed moving downward. The

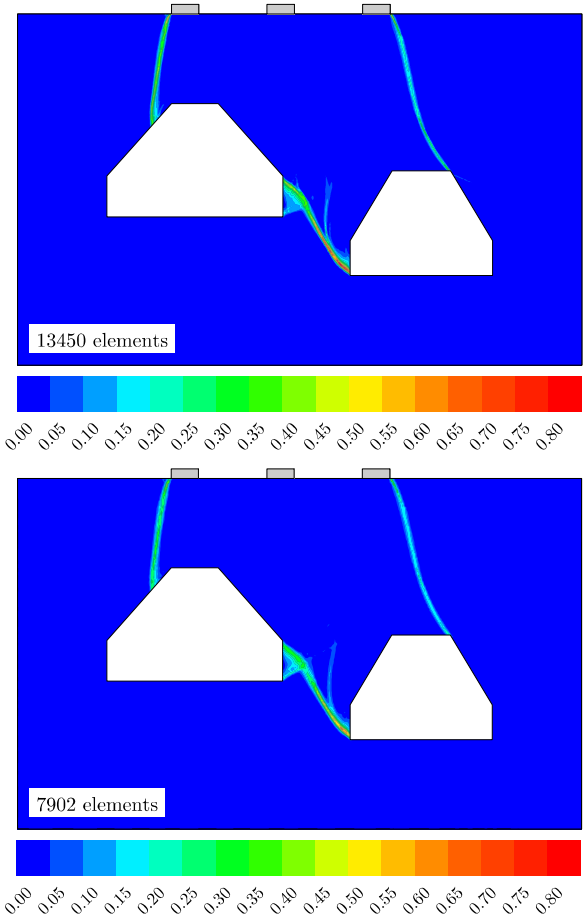

Fig. 15 Contours of shear strain of the analysed case (unweathered) for different meshes with the nonlocal model (displacement-controlled).

mechanism is more evident in Fig. 16, showing the deformed mesh for the nonlocal analysis with 7902 elements.

4.3 Obtained results - mesh independence in load-controlled simulations

As previously mentioned, the displacement-controlled simulations do not represent a realistic loading condition. Therefore, remaining analyses were performed by increasing uniformly distributed loads at the location of the foundations. The maximum capacity was assessed in terms of the total applied force (per unit width) vs the mean vertical displacement, i.e. the average displacement of the three foundations. Under this loading procedure, the softening branch of the curve cannot be followed, and convergence is not possible beyond the peak load.

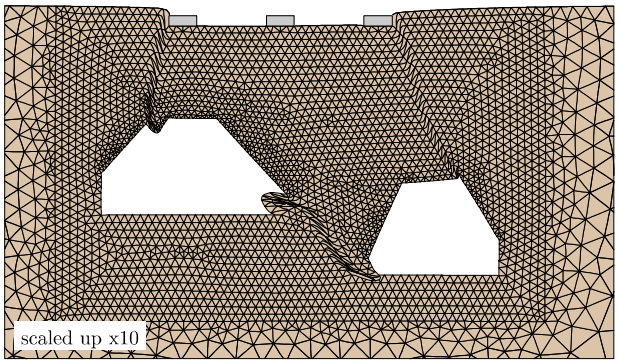

Fig. 16 Deformed mesh of the analysed case (unweathered) for the mesh with 7902 elements and with the nonlocal model (displacement-controlled).

The load-displacement curves for the unweathered case, using different meshes and the local and nonlocal models, are depicted in Fig. 17. Values of the peak load differ moderately from the displacement-controlled simulations (Fig. 12), since this loading condition induces different stress paths in the domain. However, the same conclusions can be drawn regarding the mesh dependency exhibited by the local simulations. The peak load varies as much as 72% between the different meshes with respect to the finer mesh, deeply questioning the validity of stability analyses using standard formulations for brittle materials. On the other hand, the nonlocal simulations exhibited approximately the same load-displacement curve and reached the same peak strength.

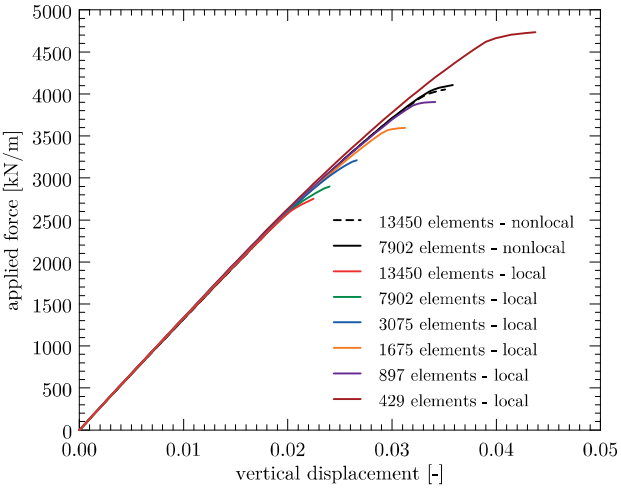

Fig. 17 Total applied force vs vertical displacement of the analysed case (unweathered) for different meshes with the local and nonlocal models (load-controlled).

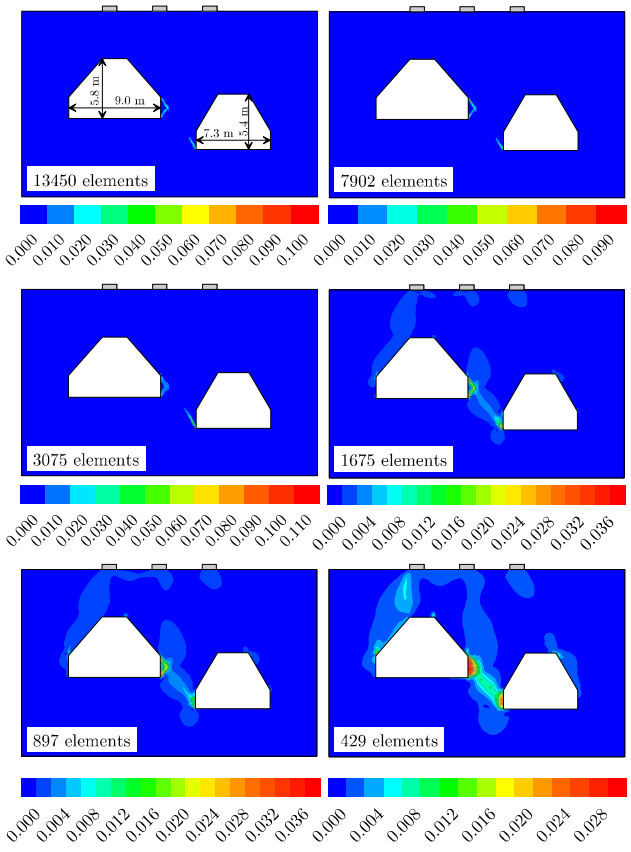

Fig. 18 Contours of shear strain of the analysed case (unweathered) for different meshes with the local model (load-controlled).

Regarding the configuration of localised deformations, Fig. 18 and 19 showed the contours of shear strain for the local and nonlocal simulations respectively. Since the amount of plastic straining is limited at reaching the peak, the failure mechanism is not yet completely defined. However, as in the displacement-controlled simulations, it initiates by the formation of a shear band in the pillar between the two caves. Unlike the load-displacement curves, the general configuration of the failure mechanism seems not to be very sensitive to the mesh in this case and appears to be controlled by the geometry of the problem. However, the thickness of the shear bands formed in the local analyses does show a clear dependency with the mesh, increasing as the size of elements is increased.

4.4 Obtained results - different softening rates

The unweathered case was also analysed for the two meshes with the nonlocal model considering two additional values for b_c: 5 and 10. The configuration of localised deformations for the additional analyses were quite similar to the nonlocal analysis with $b_c = 22$ (Fig. 19) and, therefore, they are not reported here. Nevertheless, the force-displacement curve did show significant differences (Fig. 20). Unlike the biaxial simulations, were the same peak load was attained regardless of the softening rate, the simulation of the case study resulted in different peak loads depending on the b_c values employed. A lower softening rate resulted in a larger peak load and a more ductile global response.

The differences with respect to the biaxial simulations, where the same peak load was attained, can be explained in terms of the non-uniformity of the stress/strain field. Both the biaxial simulations and the case study experience such condition. Therefore, softening is progressively attained in an increasing number of Gauss points as the simulation progresses and, therefore, they experience progressive failure. However, in the biaxial simulations, non-uniformities are modest and, therefore, only small displacements occur from

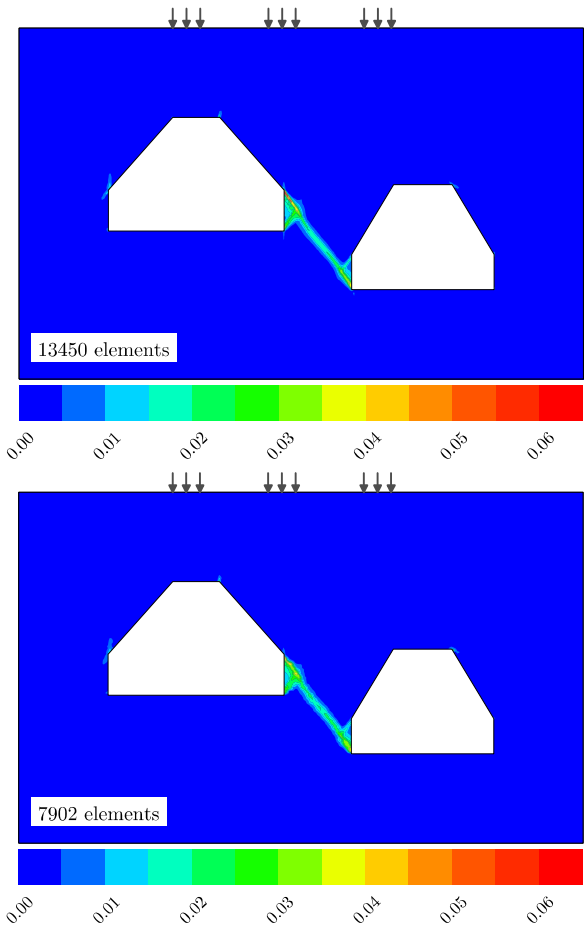

Fig. 19 Contours of shear strain of the analysed case (unweathered) for different meshes with the nonlocal model (load-controlled).

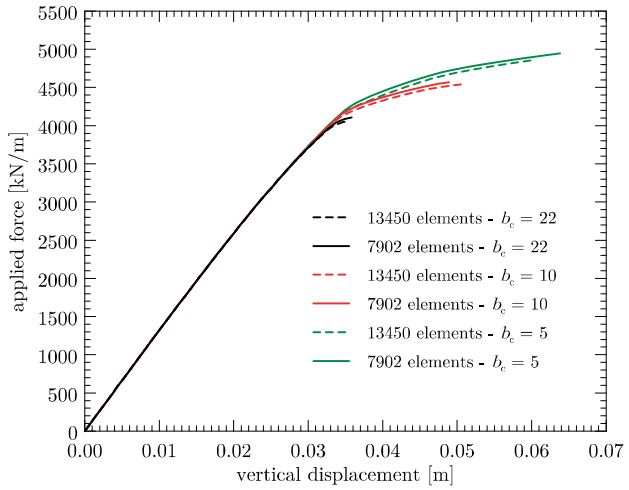

Fig. 20 Total applied force vs vertical displacement of the analysed case (unweathered) for different meshes with the nonlocal model and different values of b_c (load-controlled).

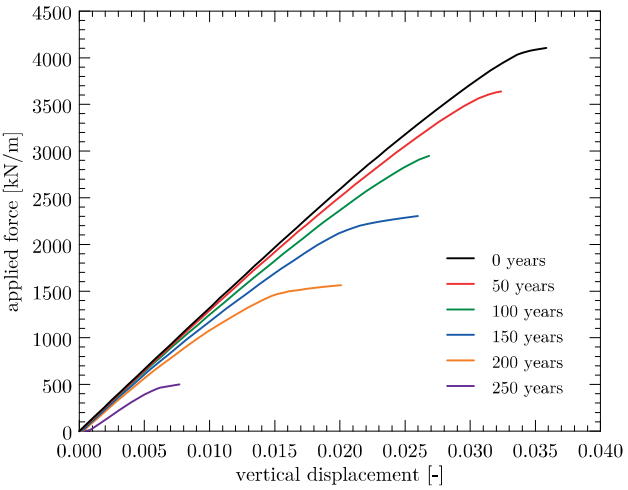

Fig. 21 Total applied force vs vertical displacement for the different weathering scenarios (load-controlled).

the instant that the first point enters into the softening regime to the moment when all points within the shear band are in the softening branch (points outside the shear band tend to unload elastically) (see Mánica et al., 2018). On the other hand, non-uniformities are larger in the case study, and softening is first concentrated in the zone in-between the caves. For larger softening rates, the strength decreases faster in this zone reducing the capacity to redistribute stresses to elements still in the elastic or hardening regime as the simulation progresses. Therefore, the global capacity of the BVP is reduced as the softening rate is increased.

From back-analysis of case histories, recommendations have been made on the operational strength to be used for stability evaluations when dealing with brittle materials (e.g. Mesri and Shahien, 2003). However, results presented here suggest that a general criterion will prove quite difficult (maybe impossible) to develop. The stability of a given engineering problem will depend not only on the values of the peak (or intact), post-peak (or fully softened), and residual strengths but also on the rate of strength loss and the non-uniformity of the generated strain/stress field for the particular problem under consideration, as suggested by Gens (2013).

4.5 Obtained results - different weathering scenarios

Analyses considering different weathering scenarios (0, 50, 100, 150, 200, and 250 years) were only performed with $b_c = 22$. The load-displacement curves obtained are shown in Fig. 21. It can be observed that the peak load reduces significantly in the 250-year period of weathering considered. The evolution with weathering time of the peak force before the lack of convergence is depicted in Fig. 22. A reduction of the peak load of 88% occurs between the initial and last scenario. This major reduction implies that a structure initially designed to fulfil the stability requirements, based on the initial state of the ground, can move to an unsafe situation if the weathering of the calcarenite is not properly controlled.

The configurations of localised deformations obtained are shown in Fig. 23. It appears that the mechanism of the unweathered case is not significantly modified in the different weathering scenarios. As indicated

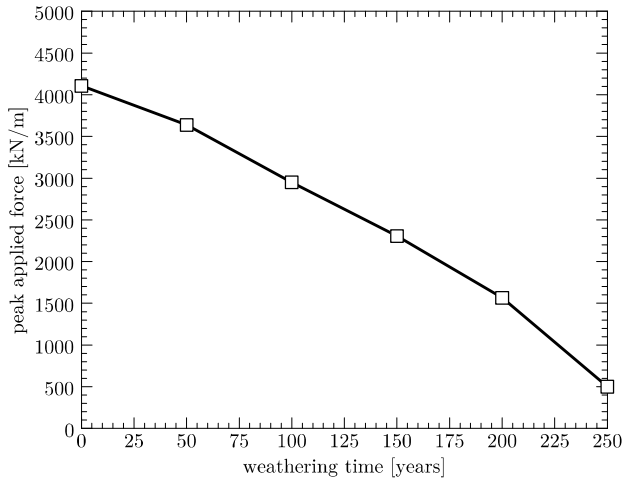

Fig. 22 Evolution of the maximum applied load for the different weathering scenarios.

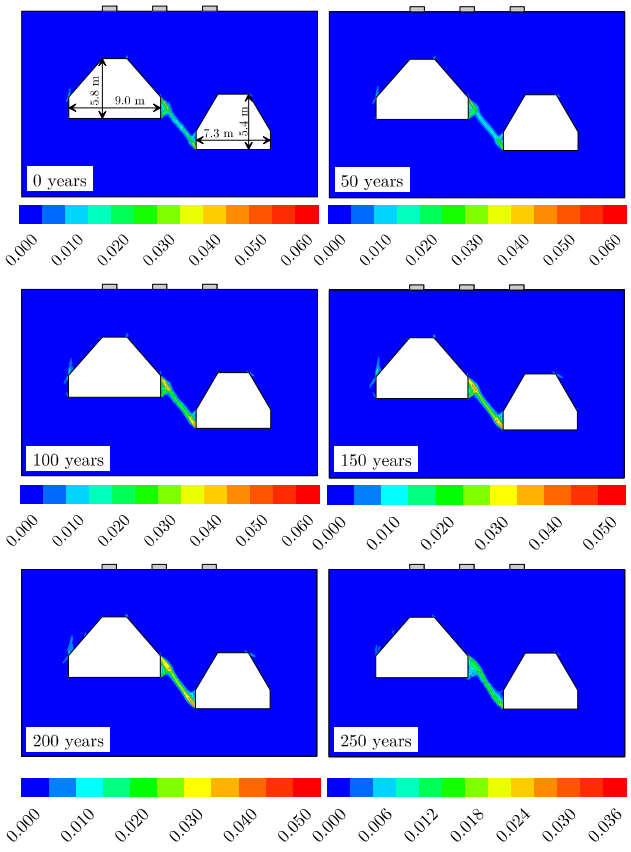

Fig. 23 Contours of shear strain for the different weathering scenarios.

above, the failure mechanism appears to be controlled by the geometry of the case study.

The considerable reduction of the foundation capacity can be explained by considering Fig. 10 and Fig. 23. The main shear failure mechanism occurs in-between the two caves even in the absence of weathering. However, when weathering is considered, a marked reduction of the strength occurs in that area making it considerably more susceptible to failure. Different sensitivity to weathering should be expected depending on the location of the dominant failure mechanism and on the degree of the exposure of the calcarenite to atmospheric conditions.

5 Conclusions

This paper addresses the effect of long-term weathering processes on the stability of a building resting on a calcarenite, where two man-made caves exist directly below the structure. As a first approximation, a one-way coupling approach was employed. The reactive transport problem was first solved and its results were fed into the mechanical problem. For the latter, a nonlocal approach was adopted for the objective simulation of localised deformations. A number of analyses were performed, from which the following conclusion can be drawn:

- Results showed a maximum reduction of the peak capacity of the foundation of 88% in the 250-year weathering period considered. This significant reduction implies that a structure initially designed to fulfil stability requirements, based on the initial state of the ground, can move to an unsafe situation if the effects of weathering are not properly controlled. The zone where the main failure mechanism occurred corresponded to a zone with large degradation due to weathering, enhancing the effects of the loss of capacity. Different sensitivity to weathering can be expected for different BVP depending on both the spatial evolution of weathering and the configuration of the failure mechanism.
- In more constrained simulations, as the BVP of a laboratory test, the peak strength is not considerably altered by the pathological mesh dependence when dealing with strain localisation, and only the post-peak behaviour is significantly affected by the mesh employed. However, in more complex BVPs, as the one analysed here, even the peak of the load-displacement curve is affected by mesh dependence. Therefore, the regularisation of the finite element solution is of the uttermost importance when assessing the stability of structures on brittle materials.
- Although the nonlocal approach can deliver objective results that do not depend on the mesh employed, the progressive failure condition, brought about by the brittle behaviour of the calcarenite, causes the maximum capacity of the problem to depend on the rate of strength loss and the non-uniformity of the generated stress/strain field for the particular problem under consideration. Furthermore, the softening rate observed in experiments depends on the particular localisation pattern obtained (and particular test conditions) and, therefore, is not an intrinsic material parameter. Due to the particularities of the regularisation technique employed, the softening rate will also depend on the length scale parameter, which is in turn related to the mesh that can be used with current computational resources. The proposal of a rational approach to determine an adequate softening rate for regularised simulations of real engineering problems, from laboratory test results, is an open problem and more research is required to incorporate this type of simulations in routine stability assessments.

– To advance in the simulation of the effects of weathering in real engineering problems, CHM coupled constitutive models, as the one described in Ciantia and di Prisco (2016), should be enhanced with some type of regularisation technique for the objective simulation of localised deformations. Moreover, the reactive transport and the hydromechanical simulations should be performed simultaneously to properly capture the coupled mechanisms and to derive a more accurate description of the behaviour of structures as weathering progresses in time.

Conflict of interest

The authors declare that they have no conflict of interest.

References

Baxevanis T, Papamichos E, Flornes O, Larsen I (2006) Compaction bands and induced permeability reduction in Tuffeau de Maastricht calcarenite. Acta Geotechnica 1(2):123–135, DOI 10.1007/s11440-006-0011-y

Bažant ZP, Jirásek M (2002) Nonlocal integral formulations of plasticity and damage: survey of progress. Journal of Engineering Mechanics 128(11):1119–1149, DOI 10.1061/(ASCE)0733-9399(2002)128:11(1119)

Bažant ZP, Oh BH (1983) Crack band theory for fracture of concrete. Matériaux et construction 16(3):155–177, DOI 10.1007/BF02486267

de Borst R, Sluys LJ, Mühlhaus HB, Pamin J (1993) Fundamental issues in finite element analyses of localization of deformation. Engineering Computations 10(2):99–121, DOI 10.1108/eb023897

Brinkgreve RBJ (1994) Geomaterials models and numerical analysis of softening. PhD thesis, Delft University of Technology

Brinkgreve RBJ, Kumarswamy S, Swolfs WM, Zampich L, Ragi-Manoj N (2019) PLAXIS 2019 user manual

Castellanza R, Lollino P, Ciantia M (2018) A methodological approach to assess the hazard of underground cavities subjected to environmental weathering. Tunnelling and Underground Space Technology 82:278–292, DOI 10.1016/j.tust.2018.08.041

Chandra S, Nilsen B, Lu M (2010) Predicting excavation methods and rock support: A case study from the Himalayan region of india. Bulletin of Engineering Geology and the Environment 69(2):257–266, DOI 10.1007/s10064-009-0252-8

Ciantia MO (2013) Multiscale hydro-chemo-mechanical modelling of the weathering of calcareous rocks: an experimental, theoretical and numerical study. Phd, Politecnico di Milano

Ciantia MO, Hueckel T (2013) Weathering of submerged stressed calcarenites: chemo-mechanical coupling mechanisms. Géotechnique 63(9):768–785, DOI 10.1680/geot.sip13.p.024

Ciantia MO, di Prisco C (2016) Extension of plasticity theory to debonding, grain dissolution, and chemical damage of calcarenites. International Journal for Numerical and Analytical Methods in Geomechanics 40(3):315–343, DOI 10.1002/nag.2397

Ciantia MO, Castellanza R, di Prisco C, Hueckel T (2013) Experimental methodology for chemo-mechanical weathering of calcarenites. In: Laloui L, Ferrari A (eds) Multiphysical Testing of Soils and Shales, springer s edn, Springer, Berlin, Heidelberg, pp 331–336, DOI 10.1007/978-3-642-32492-5_43

Ciantia MO, Castellanza R, di Prisco C (2015a) Experimental study on the water-induced weakening of calcarenites. Rock Mechanics and Rock Engineering 48(2):441–461, DOI 10.1007/s00603-014-0603-z

Ciantia MO, Castellanza R, di Prisco C, Lollino P, Merodo JAF, Frigerio G (2015b) Evaluation of the Stability of Underground Cavities in Calcarenite Interacting with Buildings Using Numerical Analysis. In: Lollino G, Giordan D, Marunteanu C, Christaras B, Yoshinori I, Margottini C (eds) Engineering Geology for Society and Territory - Volume 8, Springer International Publishing, Cham, pp 65–69, DOI 10.1007/978-3-319-09408-3_8

Ciantia MO, Castellanza R, Fernandez-Merodo JA (2018) A 3D numerical approach to assess the temporal evolution of settlement damage to buildings on cavities subject to weathering. Rock Mechanics and Rock Engineering 51(9):2839–2862, DOI 10.1007/s00603-018-1468-3

Desrues J, Viggiani G (2004) Strain localization in sand: an overview of the experimental results obtained in Grenoble using stereophotogrammetry. International Journal for Numerical and Analytical Methods in Geomechanics 28(4):279–321, DOI 10.1002/nag.338

van Eekelen HAM (1980) Isotropic yield surfaces in three dimensions for use in soil mechanics. International Journal for Numerical and Analytical Methods in Geomechanics 4(1):89–101, DOI 10.1002/nag.1610040107

Fernandez-Merodo JA, Castellanza R, Mabssout M, Pastor M, Nova R, Parma M (2007) Coupling transport of chemical species and damage of bonded geomaterials. Computers and Geotechnics 34(4):200–

215, DOI 10.1016/j.compgeo.2007.02.008

Gajo A, Cecinato F, Hueckel T (2019) Chemo-mechanical modeling of artificially and naturally bonded soils. Geomechanics for Energy and the Environment 18:13–29, DOI 10.1016/j.gete.2018.11.005

Galavi V, Schweiger HF (2010) Nonlocal multilaminate model for strain softening analysis. International Journal of Geomechanics 10(1):30–44, DOI 10.1061/(ASCE)1532-3641(2010)10:1(30)

Gens A (2010) Soil environment interactions in geotechnical engineering. Géotechnique 60(1):3–74, DOI 10.1680/geot.9.P.109

Gens A (2013) On the hydromechanical behaviour of argillaceous hard soils-weak rocks. In: Anagnostopoulos A, Pachakis M, Tsatsanifos C (eds) Proceedings of the 15th European Conference on Soil Mechanics and Geotechnical Engineering - Geotechnics of Hard Soils - Weak Rocks, IOS Press, Athens, vol 4, pp 71–118, DOI 10.3233/978-1-61499-199-1-71

Gens A, Nova R (1993) Conceptual bases for a constitutive model for bonded soils and weak rocks. In: Anagnostopoulos AG (ed) Proceedings of the international conference on hard soils - soft rocks, Balkema, Athens, vol 1, pp 485–494

Gens A, Carol I, Alonso EE (1990) A constitutive model for rock joints formulation and numerical implementation. Computers and Geotechnics 9(1-2):3–20, DOI 10.1016/0266-352X(90)90026-R

Kozicki J, Donzé FV (2008) A new open-source software developed for numerical simulations using discrete modeling methods. Computer Methods in Applied Mechanics and Engineering 197(49-50):4429–4443, DOI 10.1016/j.cma.2008.05.023

Lagioia R, Nova R (1995) An experimental and theoretical study of the behaviour of a calcarenite in triaxial compression. Géotechnique 45(4):633–648, DOI 10.1680/geot.1995.45.4.633

Lollino P, Andriani GF (2017) Role of brittle behaviour of soft calcarenites under low confinement: Laboratory observations and numerical investigation. Rock Mechanics and Rock Engineering 50(7):1863–1882, DOI 10.1007/s00603-017-1188-0

Mahabadi OK, Lisjak A, Munjiza A, Grasselli G (2012) Y-Geo: New combined finite-discrete element numerical code for geomechanical applications. International Journal of Geomechanics 12(6):676–688, DOI 10.1061/(ASCE)GM.1943-5622.0000216

Mánica MA, Gens A, Vaunat J, Ruiz DF (2018) Nonlocal plasticity modelling of strain localisation in stiff clays. Computers and Geotechnics 103:138–150, DOI 10.1016/j.compgeo.2018.07.008

Mesri G, Shahien M (2003) Residual Shear Strength Mobilized in First-Time Slope Failures. Journal of Geotechnical and Geoenvironnemental Engineering 129(1):12–31, DOI 10.1061/(ASCE)1090-0241(2003)129:1(12)

Monforte L, Ciantia MO, Carbonell JM, Arroyo M, Gens A (2019) A stable mesh-independent approach for numerical modelling of structured soils at large strains. Computers and Geotechnics 116, DOI 10.1016/j.compgeo.2019.103215

Morris JP, Rubin MB, Block GI, Bonner MP (2006) Simulations of fracture and fragmentation of geologic materials using combined FEM/DEM analysis. International Journal of Impact Engineering 33(1-12):463–473, DOI 10.1016/j.ijimpeng.2006.09.006

Nicolas A, Fortin J, Regnet JB, Dimanov A, Gúeguen Y (2016) Brittle and semi-brittle behaviours of a carbonate rock: Influence of water and temperature. Geophysical Journal International 206(1):438–456, DOI 10.1093/gji/ggw154

Nova R (1986) Soil models as a basis for modelling the behaviour of geophysical materials. Acta Mechanica 64(1-2):31–44, DOI 10.1007/BF01180096

Nova R (1992) Mathematical modelling of natural and engineered geomaterials. European Journal of Mechanics - A/Solids 11:135–154

Nova R, Castellanza R, Tamagnini C (2003) A constitutive model for bonded geomaterials subject to mechanical and/or chemical degradation. International Journal for Numerical and Analytical Methods in Geomechanics 27(9):705–732, DOI 10.1002/nag.294

Oñate E, Rojek J (2004) Combination of discrete element and finite element methods for dynamic analysis of geomechanics problems. Computer Methods in Applied Mechanics and Engineering 193(27-29):3087–3128, DOI 10.1016/j.cma.2003.12.056

Parise M, Lollino P (2011) A preliminary analysis of failure mechanisms in karst and man-made underground caves in Southern Italy. Geomorphology 134(1-2):132–143, DOI 10.1016/j.geomorph.2011.06.008

Pijaudier-Cabot G, Bažant ZP (1987) Nonlocal Damage Theory. Journal of Engineering Mechanics 113(10):1512–1533, DOI 10.1061/(ASCE)0733-9399(1987)113:10(1512)

Potyondy DO, Cundall PA (2004) A bonded-particle model for rock. International Journal of Rock Mechanics and Mining Sciences 41(8):1329–1364, DOI 10.1016/j.ijrmms.2004.09.011

Raynaud S, Vasseur G, Soliva R (2012) In vivo CT X-ray observations of porosity evolution during triaxial deformation of a calcarenite. International Journal of Rock Mechanics and Mining Sciences 56:161–170, DOI 10.1016/j.ijrmms.2012.07.020

Regueiro RA, Borja RI (2001) Plane strain finite element analysis of pressure sensitive plasticity with strong discontinuity. International Journal of Solids and Structures 38(21):3647–3672, DOI 10.1016/S0020-7683(00)00250-X

Summersgill FC, Kontoe S, Potts DM (2017) Critical assessment of nonlocal strain-softening methods in biaxial compression. International Journal of Geomechanics 17(7):1–14, DOI 10.1061/(ASCE)GM.1943-5622.0000852

Tamagnini C, Ciantia MO (2016) Plasticity with generalized hardening: Constitutive modeling and computational aspects. Acta Geotechnica 11(3):595–623, DOI 10.1007/s11440-016-0438-8

Tamagnini C, Castellanza R, Nova R (2002) A Generalized Backward Euler algorithm for the numerical integration of an isotropic hardening elastoplastic model for mechanical and chemical degradation of bonded geomaterials. International Journal for Numerical and Analytical Methods in Geomechanics 26(10):963–1004, DOI 10.1002/nag.231

Utili S, Crosta GB (2011) Modeling the evolution of natural cliffs subject to weathering: 2. Discrete element approach. Journal of Geophysical Research: Earth Surface 116(F1):1–17, DOI 10.1029/2009JF001559

Witteveen P, Ferrari A, Laloui L (2013) An experimental and constitutive investigation on the chemo-mechanical behaviour of a clay. Géotechnique 63(3):244–255, DOI 10.1680/geot.sip13.p.027

Wong TF, Baud P (2012) The brittle-ductile transition in porous rock: A review. Journal of Structural Geology 44:25–53, DOI 10.1016/j.jsg.2012.07.010

Zimbardo M (2016) Mechanical behaviour of Palermo and Marsala calcarenites (Sicily), Italy. Engineering Geology 210:57–69, DOI 10.1016/j.enggeo.2016.06.004